Quasi-CJ rotating detonation with partially premixed methane-oxygen injection: Numerical simulation and experimental validation

Pierre Hellard, Thomas Gaillard, Dmitry Davidenko, Patrick Berterretche, Ratiba Zitoun, Pierre Vidal

Applications in Energy and Combustion Science 19 (2024) 100278

Contents lists available at ScienceDirect

Applications in Energy and Combustion Science

journal homepage: www.elsevier.com/locate/jaecs

Quasi-CJ rotating detonation with partially premixed methane-oxygen injection: Numerical simulation and experimental validation

Pierre Hellard [a], Thomas Gaillard [a], Dmitry Davidenko [a], Patrick Berterretche [b], Ratiba Zitoun [b], Pierre Vidal [b,*]

[a] DMPE, ONERA, University of Paris-Saclay, Palaiseau, 91120, France
[b] Institut Pprime, UPR 3346 CNRS, ENSMA, University of Poitiers, Futuroscope-Chasseneuil, 86960, France

ARTICLE INFO

Keywords:
Rotating Detonation Engine
Partial premixing
Pressure gain combustion
Large Eddy Simulation
Experiments
Rocket engine

ABSTRACT

The efficiency gain of rotating detonation depends on several loss factors related to the chamber geometry, the injection principle, the propellants and their mass flow rates, and the equivalence ratio. Numerical simulation can help quantify these losses, and this work presents a Large Eddy Simulation (LES) of rotating detonation in an annular chamber and its validation against experiments. The simulation captured the mixing processes, the overall dynamics of the detonation, the deflagration, and the burnt gas expansion. The injection device was numerically designed to ensure partial premixing of the propellants before injection into the chamber. The chamber had a length of 110 mm, an outer diameter of 80 mm, and a radial width of 10 mm. The mixture consisted of gaseous CH_4 and O_2 with an equivalence ratio of 1.2 and a mass flow rate of 160 g/s. Combustion kinetics was modeled using a skeletal mechanism with 62 reactions and 16 species. The boundary conditions were adiabatic slip walls. The results reproduce well the detonation velocity (within 1% deviation) and the pressure variation behind the wave. The simulated OH* chemiluminescence compares well with experimental high-speed imaging of the outlet and side of the chamber. The simulation results indicate that 65% of the propellant mass is well mixed in front of the wave whereas 15% of the mixture is burned by deflagration. They show that CH_4 and O_2 do not axially stratify because they have similar injection dynamics between periodic perturbations induced by the rotating detonation. Good propellant mixing and low deflagration losses explain the high experimental detonation velocity, about 90% of D_{CJ}, and a high combustion efficiency of 98%. These agreements between the computational and experimental results indicate that the simulation is capable of capturing the physical scales relevant to RDC operation and producing reliable results for RDC design.

1. Introduction

Detonation is a promising combustion mode for increasing engine performance and reducing fuel consumption. The Rotating Detonation Engine (RDE) receives today most of the attention because of its wide operating range [1], simple design [2], self-maintained combustion, and compactness [3]. However, loss factors limit the efficiency gain, some of which this study aims to quantify based on numerical simulations of a Rotating Detonation Combustor (RDC) with partially premixed injection, validated against experimental observations.

The main loss factors are incomplete mixing [4], parasitic deflagration [5,6], and unfit chamber and nozzle geometries [7–10]. For example, the detonation velocities observed in experiments are lower than the theoretical Chapman–Jouguet (CJ) values of reference because of imperfect mixing of the propellants [11,12] and burnt gas dilution [13,14]. In rocket-type RDEs, the higher reactivity of the propellant mixture increases the number of waves [15], which can limit the time available for mixing. Higher reactivity also promotes deflagration losses [16]. Therefore, these RDEs tend to have higher detonation velocity deficits than air-breathing RDEs, although rocket-type detonation applications are easier.

Several experiments and simulations showed that the dynamic response of the flow at the injector outlet can lead to an axial stratification of the mixture in front of the wave, resulting in incomplete combustion [17,18]. Insufficient mixing of the propellants may lead to combustion heat release distributed throughout the chamber instead of concentrated in the detonation front [19], thus reducing the combustion efficiency. For example, the value of 0.85 was obtained in an experimental CH_4/air RDC [20].

* Corresponding author.
E-mail address: pierre.vidal@ensma.fr (P. Vidal).

https://doi.org/10.1016/j.jaecs.2024.100278
Received 29 March 2024; Received in revised form 26 June 2024; Accepted 2 July 2024
Available online 15 July 2024

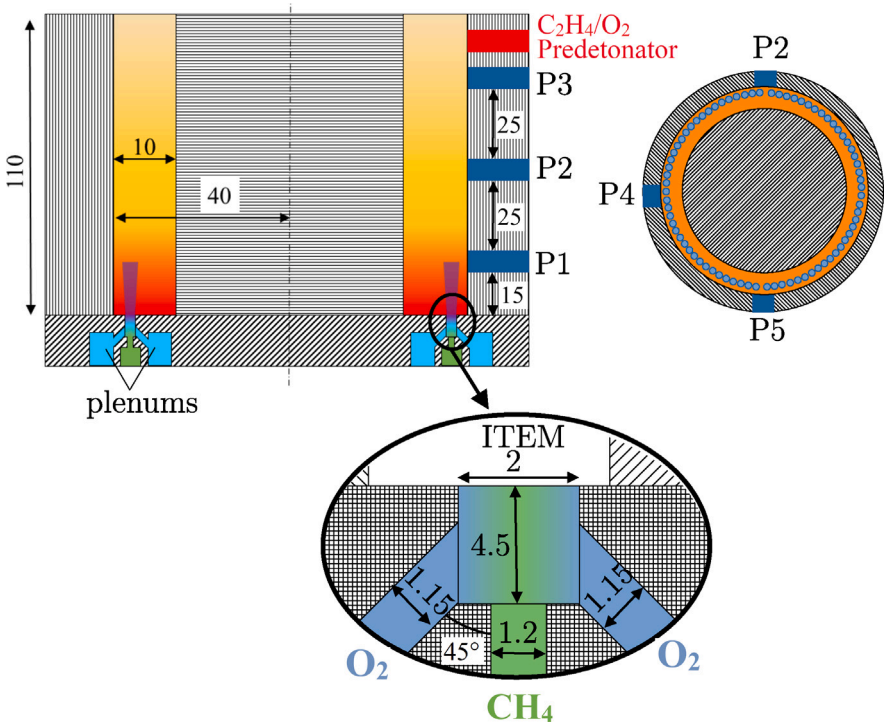

Fig. 1. Schematics of the chamber and the ITEM injector (length units are mm).

Solving mixing problems implies considering different degrees of propellant premixing. Experiments with full premixing often show deflagration, slow detonation modes, or unstable regimes [13,21]. However, it was also reported that injecting separately non-premixed H_2 and premixed C_2H_4/O_2 increased the RDC operation stability [22]. Therefore, partial premixing seems to be an interesting option providing a higher detonation velocity in hydrogen and methane-fueled RDCs [23–25] and improving the combustion efficiency in a kerosene-fueled RDC [26].

This study is an analysis of numerical simulations and their experimental validation for an RDC with partially premixed injection, operating with gaseous CH_4/O_2 at quasi-CJ velocity (D_{CJ}). Section 2 introduces the RDC and injector geometries. Section 3 describes the numerical approach and its validation by comparison with experimental observations. Section 4 presents the numerical analysis of the main phenomena in the RDC, including propellant mixing, deflagration and detonation dynamics, reinjection dynamics, and outlet flow properties.

2. Experimental set-up

The experimental set-up was an annular RDC implemented on the GAP test facility [27], with chamber length 110 mm, outer diameter 80 mm and annular width 10 mm, comparable to some other RDCs [28,29].

Fig. 1 shows the injection device, which comprised 72 evenly spaced injection elements. Each element was composed of a 2 mm-diameter prechamber that received the fuel (gaseous CH_4) from a 1.2 mm-diameter axial channel and the oxidizer (gaseous O_2) from two 1.15 mm-diameter, 45° oblique channels, arranged symmetrically to form semi-impinging jets just above the fuel orifice. The injection ring was located at a radius of 37.5 mm, i.e. closer to the outer radius of the chamber rather than at its mean radius of 35 mm. The injection element was numerically designed to control the mixing and is hereafter referred to as ITEM for Injector To Enhance Mixing.

To ensure safe operation, the rotating detonation propagating in the chamber must not be transmitted to the injector. From the canonical point of view, the chamber can be seen as a tube with a large diameter,

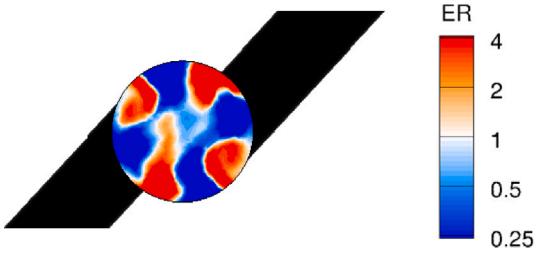

Fig. 2. Equivalence ratio at the injector outlet in a cold flow simulation. The black branches represent the semi-impinging O_2 tubes.

and the injector prechamber as a tube with a smaller diameter d. The criterion for the detonation to not propagate in the smaller tube is $d < \lambda/\pi$ [30], where λ is the detonation cell mean width [31–34]. For the perfectly-mixed stoichiometric CH_4/O_2 mixture in this work, $\lambda = 2$ mm at atmospheric pressure [35]. The safety criterion is likely met with the present 2 mm-diameter prechamber, considering that the detonation front is approximately normal to the injection plane and that cold flow simulations show incomplete mixing at the outlet of the injection prechamber (Fig. 2), which increases the characteristic chemical length and hence the expected cell width λ. Additionally, no flame can stabilize in the prechamber because the injection is sonic.

Choking throats were used to measure the fuel and oxidizer mass flow rates upstream of the injector. Five Kistler 603B high-frequency pressure transducers (P1–P5 in Fig. 1) recorded pressure signals at the chamber outer wall. Kistler 6031 pressure transducers were installed in the plenums to measure the total injection pressure. The number of waves was calculated from the phase difference between the signals of two consecutive transducers, e.g. P4 and P5, and the frequency of the main peaks from the transducer P4.

High-speed imaging of the side and back views of the RDC was performed with a Phantom TMX UV camera through a low-pass filter (550 nm), which was installed to collect OH* (308 nm) and CH* (431 nm) chemiluminescence. The spatial resolution was 312 μm/px,

Table 1
Sizes of the studied meshes.

Mesh	Medium	Refined
Tetrahedron size in the injector (μm)	60	40
Tetrahedron size in the detonation zone (μm)	150	100
Total tetrahedron number (in millions)	11	26

Table 2
Detonation velocities obtained in the experiment and the simulations with two meshes.

	Experiment	Medium	Refined
Mean detonation velocity (m/s)	2205	2196	2187
Standard deviation (m/s)	70	189	41

and the exposure time was set to 200 ns to limit the blurring effect below two pixels. Side imaging was performed through a quartz outer wall at the recording frequency of 180 kHz. For the back view, the recording frequency was 230 kHz.

3. Numerical approach and experimental validation

The main physical phenomena in RDE flows are turbulent mixing, deflagrations, detonations and shocks. Their modeling requires solving the 3D Navier–Stokes (NS) equations for compressible reactive gas, and the Large Eddy Simulation (LES) approach is well-suited for capturing turbulent flows. The NS equations were solved on an unstructured mesh with the CEDRE code [36]. A MUSCL method [37] with the Van Leer slope limiter [38] and the HLLC Riemann solver [39] provides second-order accuracy on the convective fluxes and so can capture both propellants mixing and strong gradients in the chamber. A second-order central-difference scheme was used to compute the viscous fluxes. The time integration was performed with the Euler implicit scheme and a time step of 2×10^{-9} s.

The chemical kinetics was modeled using the skeletal chemical kinetic mechanism of Laurent [40] developed for high-pressure CH_4/O_2 combustion in rocket engines, which includes 16 species and 62 reactions. Although originally developed for cryogenic initial conditions, this mechanism turns out to be valid for our conditions (Appendix).

The thermodynamic properties and the species viscosity were calculated as functions of temperature using the NASA polynomial fits and the Sutherland law [41], respectively. Species heat conduction and diffusion coefficients were calculated by assuming constant Prandtl and Schmidt numbers. The Smagorinsky subgrid approach [42] was employed to model the unresolved turbulent structures. Two unstructured meshes, having different tetrahedron sizes in the injector and the detonation propagation zone, were used (Table 1). The mesh was progressively coarsened 20 mm above the injection plane from 150 μm (Medium) or 100 μm (Refined) to 800 μm size. The size Δ of a tetrahedron was calculated from its volume V and total surface area A with the relation $\Delta = 6V/A$.

Fig. 3 shows the computational domain. Manifolds are connected to the injection elements to act as buffers for attenuating the shocks coming from the chamber and to limit their influence on the inlet conditions. The flow from the RDC is discharged into a large volume at atmospheric pressure to eliminate the influence of the outlet boundary condition on the flow. A non-reflecting, constant-pressure condition is set at the boundaries of this volume. A half of the RDC with periodic boundary conditions was considered for the simulation because two equidistant co-rotating waves were observed in the corresponding experiment. Fig. 4 presents the measured pressure signal at P1 (blue) and the same curve with a phase delay of one detonation period (red). Hence, each pair of blue and red peaks represents two different detonation fronts. It shows that the two co-rotating detonations have similar strength (peak pressure of ≈5 bar) and velocity (±70 m/s).

The total temperature (293 K) and the mass flow of each reactant were set at the inlet of the manifolds connected to the tubes feeding the injector. Resolution of the turbulent boundary layer requires highly refined meshes and computational resources which could not be allocated in this work. However, numerical studies suggest that wall friction and heat transfer have little impact on the detonation velocity in RDCs (≈3% difference) [43,44]. Therefore, the present simulations assumed adiabatic and slip walls.

A 2D simulation of the RDC with premixed injection was realized to obtain an initial condition in the RDC. This 2D computational setup is similar to that detailed in [18]. The 2D flow field was then interpolated onto the 3D RDC domain. For the injector, the initial condition was provided by a RANS simulation of the cold flow in the RDC.

The spatial resolution of the numerical approach in this work will not capture the cellular structure of a detonation wave propagating in a homogeneous mixture. In RDCs, the detonation dynamics depend mainly on the mixture, temperature, and pressure non-uniformities and gradients [45,46], and the chamber curvature [47–49]. These phenomena were taken into account in the simulation, which, therefore, should be able to reproduce these dynamics without solving the cellular structure. The following discussion aims to validate this approach based on experimental observations.

Experiments using CH_4/O_2 mixtures with a chamber mass flux ranging from 35 to 80 kg/m^2/s and equivalence ratios ER from 0.8 to 1.2 were carried out, resulting in detonation velocities D/D_{CJ} ranging from 0.85 to 0.9 (Fig. 5). The CJ velocity D_{CJ} was calculated at atmospheric pressure and room temperature for each ER. The operating condition selected for the simulations is a mass flow rate of $\dot{m} = 160$ g/s (chamber mass flux of 73 kg/m^2/s) and $ER = 1.2$, typical of the experimental cases with two stable co-rotating waves.

Table 2 compares the experimental and numerical mean detonation velocities and their standard deviations calculated from high-frequency pressure measurements in the chamber. Both meshes give detonation velocities very close to the mean experimental value, i.e. with less than 1% difference. Refining the mesh provides much better agreement with the experimentally determined standard deviation of detonation velocity, so this case was further used for detailed validation.

A numerical sensor was positioned at the same location as the transducer P1. The numerical signal was processed to account for the spatial averaging of the experimental signal due to the transducer radius $d_s = 5$ mm. This correction consisted in averaging the data recorded by the numerical sensor. Each data point of rank k was averaged over the window $[k - n/2; k + n/2]$, corresponding to the time the detonation takes to cross the experimental transducer diameter. The window width n was defined by $n = d_s f_s / D$, where f_s is the acquisition frequency of the numerical sensor. The correction only accounts for the spatial averaging in the azimuthal direction because the effect of the averaging in the axial direction is supposed to be smaller.

Fig. 6 -left compares the experimental and corrected numerical pressure signals. The simulation well reproduces the detonation velocity and the pressure peak intensity, but also the burnt gas expansion dynamics behind the detonation front, in particular a secondary shock. Indeed, the numerical pressure contour in Fig. 6 -right shows a very stiff gradient close to the end of a supersonic zone, at the angular position $\theta = 36°$.

Previous studies of CH_4/O_2 flames [50,51] have shown that the main species involved in chemiluminescence are OH* and CH*, but the skeletal reaction mechanism of Laurent [40] used in the present simulations does not include these radicals. However, Kathrotia [52] developed two sub-mechanisms to embed the chemiluminescent species OH* and CH* in detailed mechanisms. For reduced mechanisms, the Quasi-Steady State Approximation (QSSA) provides algebraic relations between the species concentration in such mechanisms and OH* and CH* [53]. In the present work, this approximation was used to post-process the simulation results. All species involved in the OH* sub-mechanism, excepting OH*, are present in the mechanism of Laurent, but not those of the CH* sub-mechanism. Therefore, only OH*

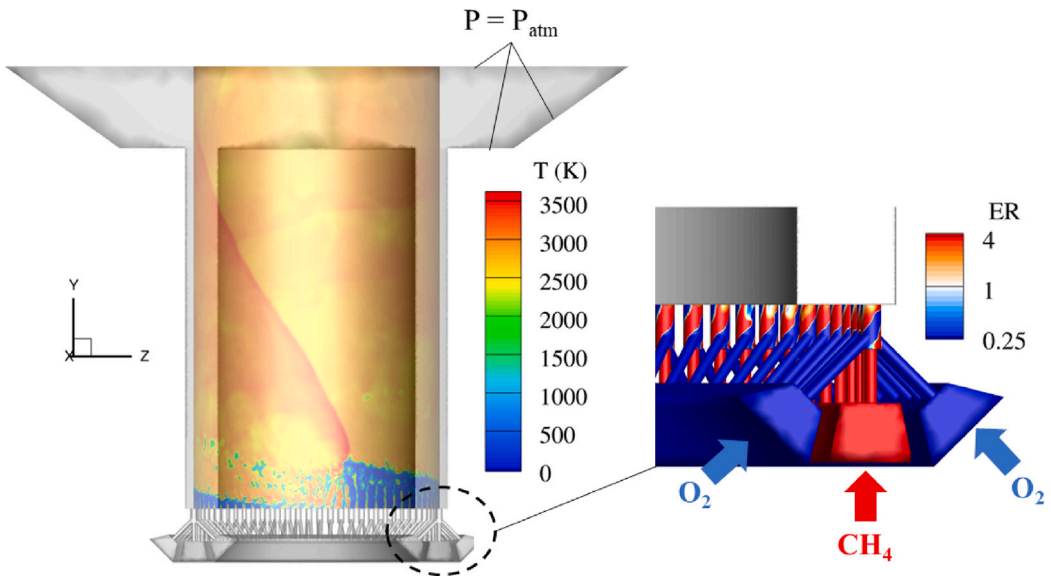

Fig. 3. Computational domain with an instantaneous temperature field at the chamber radius $R = 37.5$ mm (left) and an equivalence ratio field in the injector (right).

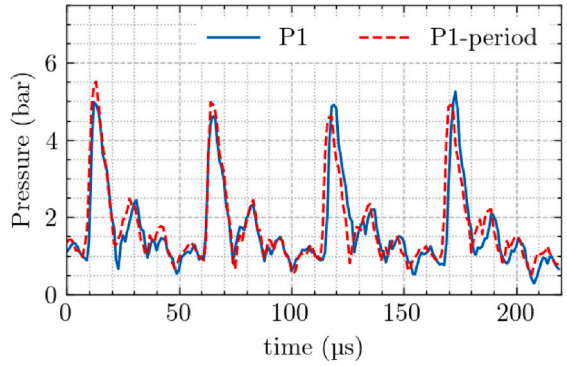

Fig. 4. Experimental pressure signals at P1. The red curve has a phase delay of one period compared to the blue curve. (For interpretation of the references to color in this figure legend, the reader is referred to the web version of this article.)

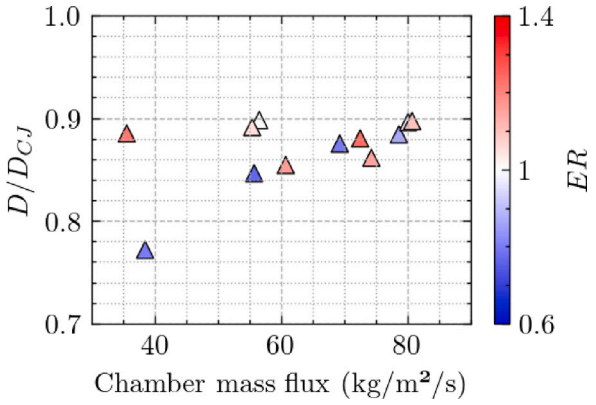

Fig. 5. Experimental detonation velocity ratio with CH_4/O_2.

concentration is evaluated using the QSSA with the mechanism of Laurent.

Calculations were performed on a canonical premixed laminar flame and a planar ZND detonation to assess the accuracy of the QSSA approach for OH* and to verify that the chemiluminescence of OH* and CH* occurs approximately in the same zone. Reference profiles for OH* and CH* were thus obtained using the GRI-Mech 3.0 detailed mechanism [54] extended with the two sub-mechanisms by Kathrotia. The results with the mechanism of Laurent were post-processed as described above. Fig. 7 shows that the CH* and OH* emission zones are practically superimposed. However, the skeletal mechanism with the QSSA underestimates the OH* concentration in both cases, and in the detonation front, the CH* concentration is much higher than that of OH*. Therefore, the comparison between experimental and simulated chemiluminescence in the RDC is only qualitative.

Fig. 8-top compares experimental (5000 frames) and simulated (30 instantaneous fields) phase-averaged chemiluminescence back-end imaging. The background noise caused by the hot gas jet was subtracted from the experimental image, and the numerical chemiluminescence was axially averaged over the chamber length, assuming proportionality between the chemiluminescence intensity and OH* radical concentration [55]. The detonation front (1) is shown as the brighter zone near the outer wall, located approximately on the ring of injection holes (Section 2). A shock wave (2) propagates in the burnt gas closer to the inner wall, and induces a lower level of chemiluminescence. The non-homogeneous chemiluminescence behind the detonation front probably results from shocks reflected at the inner and outer walls.

Fig. 8-bottom compares experimental (5000 frames) and simulated (30 instantaneous fields) phase-averaged chemiluminescence side imaging. The numerical chemiluminescence is averaged over the annular width. The well-known flow field in RDEs is retrieved, with the detonation wave (3) propagating near the injection wall, the oblique shock (4), and the attached slip line (5). The experimental and the numerical fields are similar, with a 15 mm-high detonation front and a low light emission from the parasitic deflagration in front of the detonation wave. The experimental detonation front is slightly tilted due to the non-uniform fresh mixture state in front of it, which the simulation does not reproduce. Overall, the simulation reproduces the experimental observations, including the detonation propagation velocity, the wave structure, and the burnt gas expansion.

4. Numerical analysis

The numerical results validated above are further analyzed below in three parts, although the phenomena they describe are interrelated, despite their length scales being very different. The LES cut-off length scale is within the scale range of the mixing processes – $\mathcal{O}(10-100)$ μm – so the simulation also captures the detonation and deflagration overall

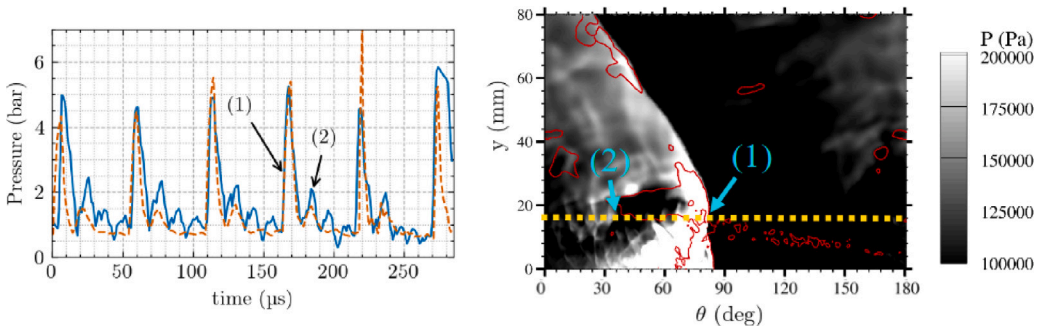

Fig. 6. Left: experimental (blue) and corrected simulated pressure (orange) signals. Right: Numerical pressure field (grey scale) at the outer wall, with the sonic isoline shown in red and the location of the transducer P1 as the yellow line. (1): detonation front, (2): secondary shock. (For interpretation of the references to color in this figure legend, the reader is referred to the web version of this article.)

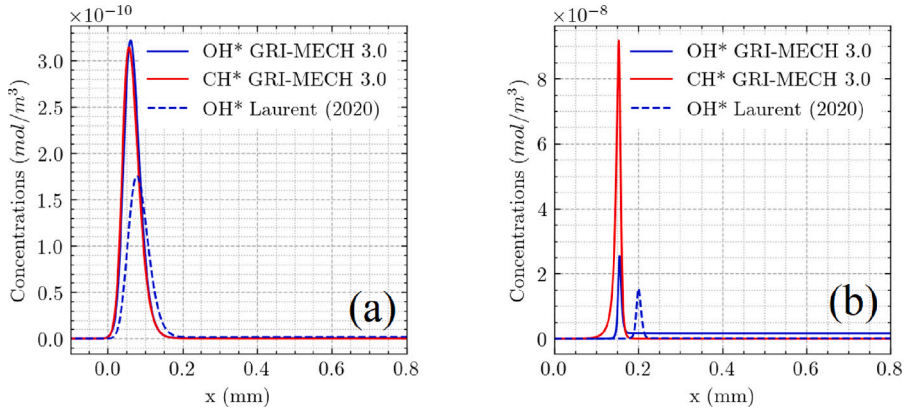

Fig. 7. Molar concentrations of OH* and CH* radicals in a 1D laminar flame (left) and a ZND detonation (right), obtained using the detailed GRI-Mech 3.0 with the Kathrotia sub-mechanism, and the skeletal mechanism of [40] with QSSA for OH*.

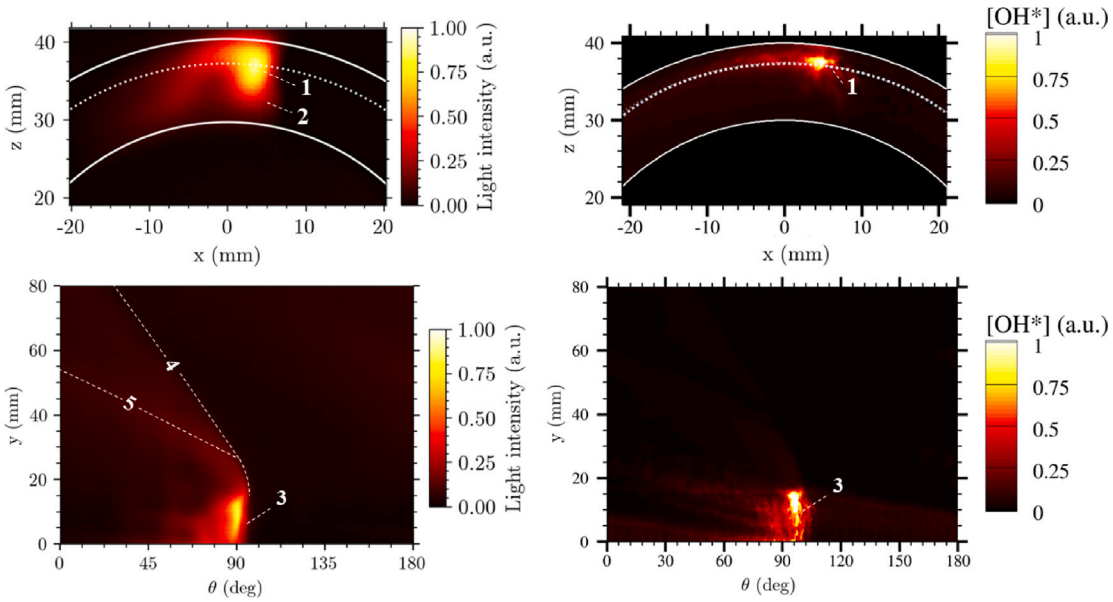

Fig. 8. Phase-averaged chemiluminescence imaging. Left: experiments, right: simulations. Top: back-end view, bottom side view. 1 & 3: detonation front. 2: oblique shock induced by the radial expansion. 4: oblique shock induced by the axial expansion. 5: slip line.

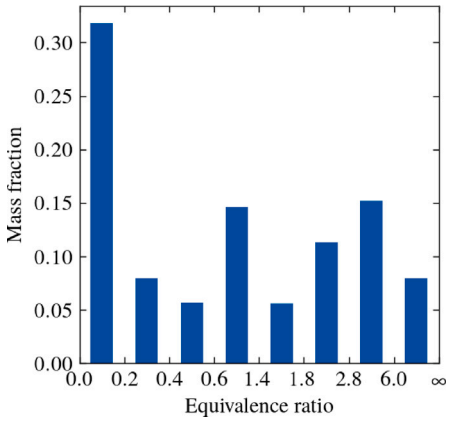

Fig. 9. Distribution of the fresh mixture mass fraction at the injector outlet.

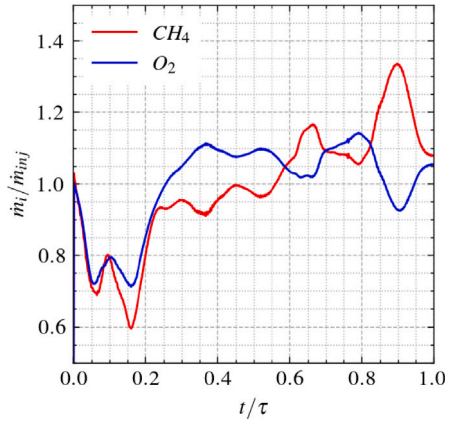

Fig. 10. Phase-averaged CH_4 and O_2 injected flow rates.

dynamics – $\mathcal{O}(0.1-10)$ mm – and the burnt gas expansion – $\mathcal{O}(1-10)$ cm. The first part details the composition of the injected mixture at the injector outlet and its response to the periodic blockage by the passage of the detonation. The second part focuses on the mixing processes in the chamber, with emphasis on the composition of the fresh mixture consumed by the detonation. The third part describes the flow field at the chamber outlet and discusses the combustion efficiency obtained with the numerically optimized ITEM injector.

4.1. Partial premixing and flow dynamic response in the injector

The simulation was used to assess the degree of premixing at the injector outlet. Fig. 9 shows the distribution of the mixture mass fraction as a function of ER over 5 detonation rotations. Only about 15% of the propellant is near stoichiometry ($0.6 < ER < 1.4$), while 33% is very lean ($ER < 0.1$), and 21% rich ($ER > 2.8$). This low mixing level prevents the combustion from propagating to the prechamber.

The injection dynamics were obtained for the flow injected through 4 evenly distributed injection elements, during 5 detonation periods, resulting in 20 reinjection cycles. Fig. 10 shows the resulting phase-averaged flow rates $\dot{m}_i$ of each propellant normalized by their respective averaged mass flow rates $\dot{m}_{inj} = \dot{m}/n_{inj}$, where $\dot{m}$ is the propellant total mass flow rate and $n_{inj} = 72$ is the number of injection elements (Section 2). The instant $t = 0$ corresponds to the detonation arrival at the injection hole and τ is the cycle period. First, the high pressure generated by the detonation passage significantly reduces the mass flow rates during 15% of the cycle period. Then, the flow rate of O_2 increases from 0.75 to stabilize around its mean value, while the flow rate of CH_4 slowly increases from 0.6 to about 1.2. Finally, the flow rate of CH_4 suddenly increases and that of O_2 decreases at the same time ($t/\tau = 0.9$), resulting in a higher injected ER. This is due to a large pocket of CH_4 generated by the interaction of the fuel and oxidizer flows in the prechamber (Section 4.2) which reduces the surface available for the O_2 injection. Overall, except for the last 10% of the cycle, O_2 and CH_4 have similar injection responses, so the mixture should not be axially stratified in the chamber.

4.2. Jet structure and mixing in front of the detonation

In previous studies [21,56], the phase-averaged mean-field was determined by moving the RDC flow field to always place the detonation at exactly the same position. This method sharpens the detonation front, but loses the detail in the fresh mixture layer. Nassini [57] proposed the Phase-Locked Ensemble Averaged method, which consists in moving the flow field to match injection element positions during one detonation period. In this case, the structure of the fresh mixture in front of the wave is preserved, but the detonation front is smeared. The same principle is used here for multiple periods.

Fig. 11-left shows the azimuthal velocity (V_θ) field and isolines of the pressure gradient over the 10 injection elements closest to the detonation front at three chamber radii R. The velocity field indicates that the ITEM injector induces significant variations of V_θ near the injection plane, which promotes mixing. The high positive values of V_θ at $R = 36$ mm near $\theta = 90°$ are due to the oblique shock associated with the detonation front propagating near the inner wall (Section 3). The pressure gradient at $R = 37.5$ mm shows, as expected, Mach barrel structures within the propellant jets, confirming that the jets are under-expanded.

Regarding the mixing, Fig. 11-right shows the ER field and the temperature isoline $T = 1000$ K in front of the detonation wave. This isoline helps to define the outer boundary of the fresh mixture layer. Above 10 mm, the mixture appears almost homogeneous, especially at the injection radius ($R = 37.5$ mm). The CH_4 unmixed pocket mentioned above (Section 4.1) is observed at $\theta < 120°$ and $R = 37.5$ mm. The axial injection from closely spaced injection orifices ensures a continuous fresh gas layer with almost no hot gases between the jets. Only at the top of the layer, near the outer wall ($R = 39$ mm), is the mixture too rich. In the main, the axial stratification is low.

Fig. 12 shows the profiles of the equivalence ratio ER and mixing efficiency η_{mix} in front of the detonation wave, confirming the low axial stratification. The mixing efficiency is convenient for quantifying the fresh mixture composition in front of the detonation. At a given axial coordinate y, it is defined as the mass fraction of propellants at the proportion corresponding to the global ER, i.e.

$$\eta_{mix}(y) = \frac{\iint_{S_y} \rho \min(Y_{CH4} + Y_{CH4} MR, Y_{O2} + Y_{O2}/MR)\, dS}{\iint_{S_y} \rho dS}, \tag{1}$$

where MR is the mixture ratio (≈3.33 here),

$$MR = \frac{2M_{O_2}}{M_{CH_4} ER_{glob}}, \tag{2}$$

M_i the molar mass of species i, ER_{glob} the global equivalence ratio ($ER_{glob} = 1.2$), ρ the mixture density, and Y_i the mass fraction of species i.

The surface S_y used for integration is bounded radially by the inner and outer walls, azimuthally on one side by the detonation front, and is $\theta = 360/n_{inj} = 5°$ wide. η_{mix} increases from 0.3 to 0.6 at the top of the fresh gas layer ($y = 13$ mm).

The total mass consumed by the detonation was obtained by integrating the mass of the fresh mixture over S_y and along y. Thus,

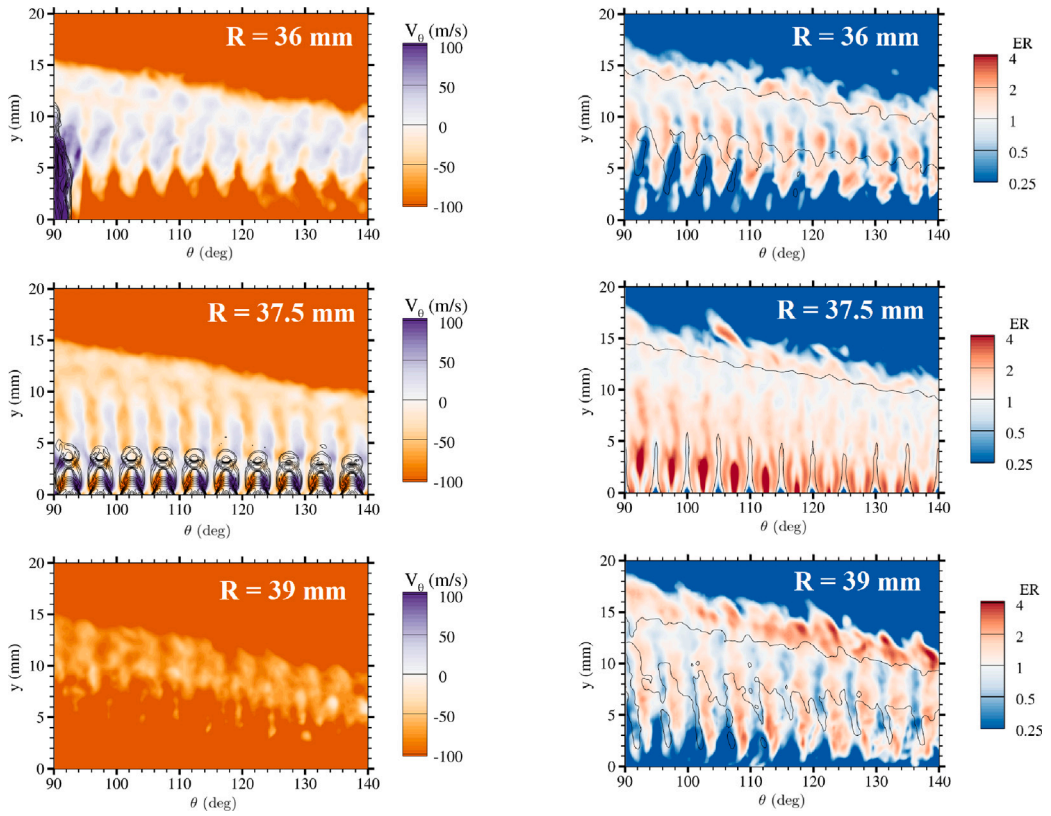

Fig. 11. Phase-averaged fields at three chamber radii. Left: Azimuthal velocity with isolines of pressure gradients. Right: ER fields with the T = 1000-K isoline.

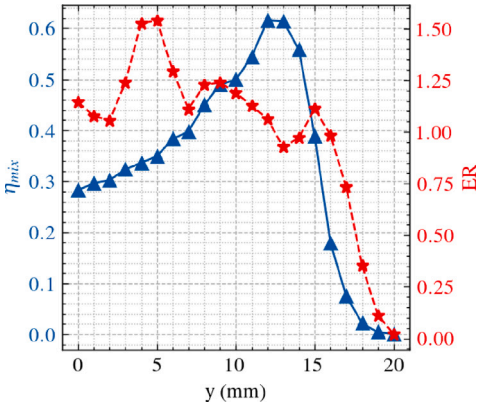

Fig. 12. Mixing efficiency and ER in front of the wave vs. the distance y to the injection plane.

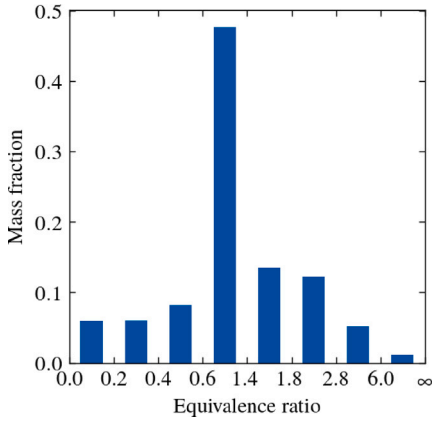

Fig. 13. Mass fraction distribution as a function of the equivalence ratio ER.

60% of the injected mass is perfectly mixed, 25% is unmixed, and the remaining 15% is burned by deflagration.

Fig. 13 shows the distribution of the mixture mass fraction as a function of ER. Most of the fresh mixture is close to stoichiometry ($0.6 < ER < 1.4$). Therefore, the good mixing quality and the low level of stratification here explain the high experimental detonation velocity, i.e. $D \approx 0.9 D_{CJ}$ (Section 2).

4.3. Flow structure, dynamics and thermodynamics at the chamber outlet

The flow at the chamber outlet was characterized by the phase and radially averaged pressure and velocity components. Information on the pressure and flow velocities at the outlet is useful for designing nozzles.

Fig. 14 shows the pressure and velocity jumps induced by the oblique shock at the angular position $\theta = 90°$. The pressure increases by 40% from 1 to 1.4 bar, the axial velocity V_y decreases from 900 to 600 m/s, and the azimuthal velocity V_θ varies from −130 to 200 m/s. However, these numbers do not include boundary layer effects.

Combustion efficiency for rocket engines is usually quantified by a ratio of characteristic velocities at the nozzle throat [58]. Since the RDC had no throat in this study, the efficiency was characterized by the ratio

$$\eta_T = \frac{\bar{T}_t}{T_{ad}} \tag{3}$$

of the mass flow averaged total temperature $\bar{T}_t$ to the isobar adiabatic combustion temperature T_{ad}. The adiabatic temperature was calculated

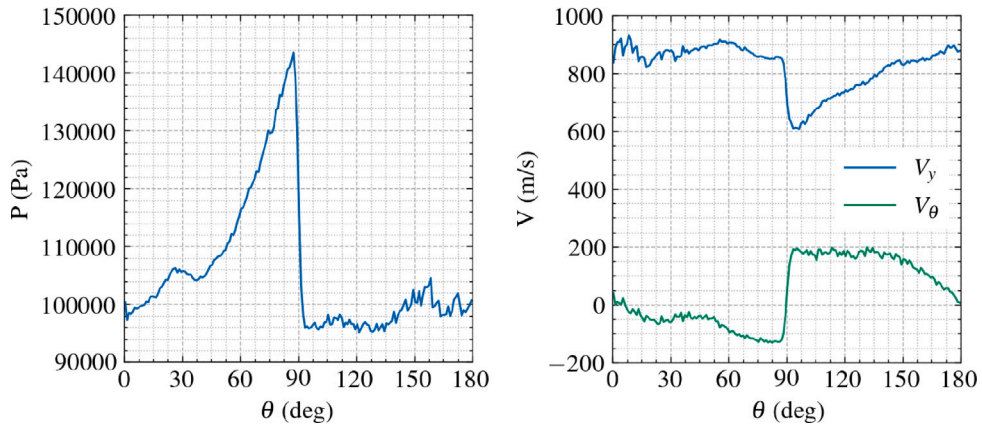

Fig. 14. Radially and phase averaged pressure (left) and velocity (right) at the chamber outlet. V_y: axial velocity. V_θ: azimuthal velocity.

using the CANTERA software [59] and the skeletal mechanism [40], assuming that the fresh gases are at the injector plenum pressure $P = 7$ bar and room temperature.

This gives $\eta_T = \bar{T}_t/T_{ad} = 0.98$, indicating that the combustion is completed in the chamber. The same value is obtained 30 mm upstream from the chamber outlet, which suggests improving compactness by shortening the chamber. Combustion completeness can also be evaluated by tracking unburnt CH_4 at the outlet. Here, there is less than 0.03% of the injected CH_4 left at 80 mm to the outlet, i.e. 30 mm from the injection plane.

5. Discussion and conclusion

The simulation of RDCs requires the capture of three main scales, namely the mixing processes, the detonation and deflagration dynamics, and the burnt gas expansion. This work validates an LES approach against experimental observations and then presents an analysis of parameters that are difficult to access experimentally.

Experimental chemiluminescence imaging provides information on the axial and radial distribution of the fresh mixture and its mixing quality. Both numerical and experimental chemiluminescence imaging show a 15 mm-high detonation front close to the injection plane, at the position of the injection ring. The numerical simulation also indicates that the fuel and oxidizer have similar injection dynamics, hence a low stratification in the chamber. The injection is reduced over 15% of the detonation period. However, when the injection regime is recovered, the under-expanded propellant jets generate significant total pressure losses, so future injector designs should consider larger injection surfaces to achieve subsonic injection.

The simulation reproduces well the wave configurations and dynamics, particularly the quasi-CJ velocities obtained in the experiments with the numerically designed ITEM injector. The analysis shows that most of the mass is burned by the detonation, so the deflagration only has a low parasitic effect on efficiency.

The numerical and experimental pressure signals are in agreement, showing, in particular, the peaks of the detonation, and of the secondary shock due to the expansion of the burnt gas. The high combustion efficiency at the outlet suggests that the chamber length could be shortened without significant losses in performance. However, the adiabatic and slip-wall assumptions overestimate the numerical chemiluminescence at the walls and may not give the right flow dynamics at the chamber outlet, i.e. an underestimated azimuthal momentum.

Prediction of the experimental detonation velocity in an RDC with non-premixed injection is challenging [19,60–64] because of the variety of phenomena that need to be captured, i.e. mixing, deflagration, detonation, burnt gas dynamics. The detonation velocity was often over-predicted and attributed to the neglect of viscous wall interactions. The present results and some previous simulations [65] tend to contradict this conclusion. Since the same assumption is implemented in the present work, a possible explanation can be the combination of the optimized injector design and the effect of a chemical kinetic mechanism well suited to thermodynamic conditions in RDCs.

CRediT authorship contribution statement

Pierre Hellard: Writing – review & editing, Writing – original draft, Visualization, Validation, Software, Investigation, Formal analysis, Conceptualization. **Thomas Gaillard:** Writing – review & editing, Validation, Supervision, Software, Project administration, Funding acquisition, Formal analysis, Conceptualization. **Dmitry Davidenko:** Writing – review & editing, Validation, Supervision, Software, Methodology, Investigation, Funding acquisition, Formal analysis, Conceptualization. **Patrick Berterretche:** Writing – review & editing, Visualization, Methodology, Investigation. **Ratiba Zitoun:** Writing – review & editing, Validation, Supervision, Project administration, Investigation, Funding acquisition, Formal analysis, Conceptualization. **Pierre Vidal:** Writing – review & editing, Validation, Supervision, Project administration, Investigation, Funding acquisition, Formal analysis, Conceptualization.

Declaration of competing interest

The authors declare that they have no known competing financial interests or personal relationships that could have appeared to influence the work reported in this paper.

Data availability

Data will be made available on request.

Acknowledgments

This study was funded by the General Scientific Direction of ONERA and the Region Nouvelle Aquitaine. The experiments were performed on the RDE of the GAP facility of the Pprime Institute, funded by the EQUIPEX program ANR-11-EQPX-0018 of the French Government. The simulation was performed using HPC resources from GENCI-IDRIS (Grant 2023-A0142B14179).

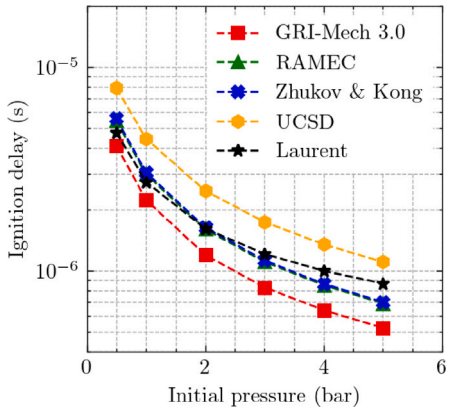

Fig. 15. Ignition delay behind a shock propagating at D_{CJ} in the stoichiometric CH_4/O_2 mixture at 300 K versus initial pressure.

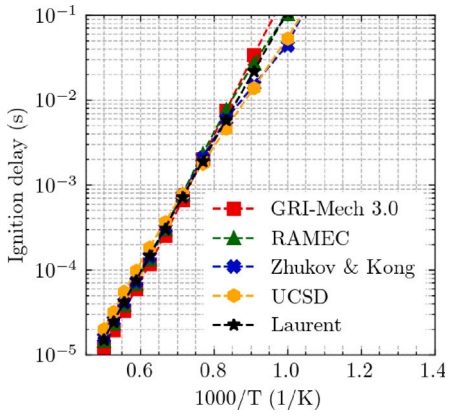

Fig. 16. Ignition delay for the stoichiometric CH_4/O_2 mixture at 1 bar versus the reciprocal of the initial temperature.

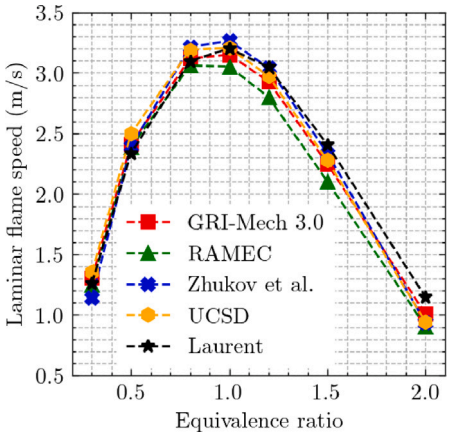

Fig. 17. Laminar flame speed for the CH_4/O_2 mixture initially at 300 K and 1 atm versus the equivalence ratio.

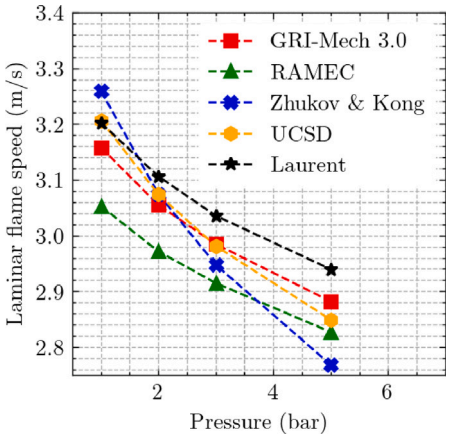

Fig. 18. Laminar flame speed for the stoichiometric CH_4/O_2 mixture initially at 300 K versus the initial pressure.

Appendix

The skeletal mechanism of Laurent [40] was validated for our conditions by comparing its predictions of ignition delay and laminar flame speed with those of the detailed mechanisms GRI-Mech3.0 [54], RAMEC [66], Zhukov and Kong [67] and UCSD [68]. The calculations were realized with CANTERA [59].

Fig. 15 shows the ignition delay behind a shock propagating at D_{CJ} in the stoichiometric CH_4/O_2 mixture initially at room temperature. The results are plotted versus the pressure in front of the shock.

Fig. 16 shows the ignition delay (at constant volume) for the stoichiometric CH_4/O_2 mixture at atmospheric pressure and various initial temperatures. The results are plotted versus the reciprocal of the initial temperature.

Fig. 17 shows the laminar flame speed for CH_4/O_2 mixtures with various equivalence ratios initially at room temperature and atmospheric pressure. The results are plotted versus the equivalence ratio.

Fig. 18 shows the laminar flame speed for the stoichiometric CH_4/O_2 mixture at various pressures and room temperature. The results are plotted versus the reciprocal of the initial pressure.

The comparison shows that the mechanism of Laurent gives satisfactory predictions for our conditions, although this mechanism was originally developed for cryogenic conditions.

References

[1] Wolański P. Detonative propulsion. Proc Combust Inst 2013;34(1):125–58.
[2] Zhdan SA, Mardashev AM, Mitrofanov VV. Calculation of the flow of spin detonation in an annular chamber. Combust Explos Shock Waves 1990;26:210–4.
[3] Heister SD, Smallwood J, Harroun A, Dille K, Martinez A, Ballintyn N. Rotating detonation combustion for advanced liquid propellant space engines. Aerospace 2022;9(10):581.
[4] Burr JR, Paulson E. Thermodynamic performance results for rotating detonation rocket engine with distributed heat addition using cantera. In: AIAA propulsion and energy 2021 forum. 2021, p. 3682.
[5] Strakey P, Ferguson D, Sisler A, Nix A. Computationally quantifying loss mechanisms in a rotating detonation engine. In: 54th AIAA aerospace sciences meeting. 2016, p. 0900.
[6] Kaemming T, Fotia ML, Hoke J, Schauer F. Thermodynamic modeling of a rotating detonation engine through a reduced-order approach. J Propuls Power 2017;33(5):1170–8.
[7] Bykovskii FA, Mitrofanov V. Detonation combustion of a gas mixture in a cylindrical chamber. Combust Explos Shock Waves 1980;16(5):570–8.
[8] Fotia M, Kaemming TA, Hoke J, Schauer F. Study of the experimental performance of a rotating detonation engine with nozzled exhaust flow. In: 53rd AIAA aerospace sciences meeting. 2015, p. 0631.
[9] Liu X-Y, Cheng M, Zhang Y-Z, Wang J-P. Design and optimization of aerospike nozzle for rotating detonation engine. Aerosp Sci Technol 2022;120:107300.
[10] Hansmetzger S, Zitoun R, Vidal P. A study of continuous rotation modes of detonation in an annular chamber with constant or increasing section. Shock Waves 2018;28:1065–78.
[11] Ishii K, Kojima M. Behavior of detonation propagation in mixtures with concentration gradients. Shock Waves 2007;17:95–102.
[12] Liu X-Y, Luan M-Y, Chen Y-L, Wang J-P. Flow-field analysis and pressure gain estimation of a rotating detonation engine with banded distribution of reactants. Int J Hydrog Energy 2020;45(38):19976–88.

[13] Andrus IQ, Polanka MD, King PI, Schauer FR, Hoke JL. Experimentation of premixed rotating detonation engine using variable slot feed plenum. J Propuls Power 2017;33(6):1448–58.
[14] Prakash S, Raman V. The effects of mixture preburning on detonation wave propagation. Proc Combust Inst 2021;38(3):3749–58.
[15] Wolański P. Rotating detonation wave stability. In: 23rd international colloquium on the dynamics of explosions and reactive systems. 2011, p. 1–6.
[16] Stechmann DP, Sardeshmukh S, Heister SD, Mikoshiba K. Role of ignition delay in rotating detonation engine performance and operability. J Propuls Power 2019;35(1):125–40.
[17] Ayers ZM, Lemcherfi A, Plaehn EW, Gejji RM, Perkins HD, Roy S, Slabaugh CD, Meyer TR, Fugger CA. Simultaneous 100-kHz acetone planar laser-induced fluorescence and oh* chemiluminescence in a linear non-premixed detonation channel. Combust Flame 2022;244:112209.
[18] Gaillard T, Davidenko D, Dupoirieux F. Numerical simulation of a rotating detonation with a realistic injector designed for separate supply of gaseous hydrogen and oxygen. Acta Astronaut 2017;141:64–78.
[19] Schau KA, Oefelein JC. Numerical analysis of wave characteristics in a Methane-Oxygen rotating detonation engine. AIAA J 2023;61(1):97–111.
[20] Walters IV, Gejji RM, Heister SD, Slabaugh CD. Flow and performance analysis of a natural gas-air rotating detonation engine with high-speed velocimetry. Combust Flame 2021;232:111549.
[21] Ayers ZM, Athmanathan V, Meyer TR, Paxson DE. Variably premixed rotating detonation engine for evaluation of detonation cycle dynamics. J Propuls Power 2023;39(3):351–64.
[22] St. George AC, Driscoll RB, Anand V, Munday DE, Gutmark EJ. Fuel blending as a means to achieve initiation in a rotating detonation engine. In: 53rd AIAA aerospace sciences meeting. 2015, p. 0633.
[23] Gaillard T. Étude numérique du fonctionnement d'un moteur à détonation rotative (Ph.D. thesis), Université Paris Saclay (COmUE); 2017.
[24] Stechmann DP. Experimental Study of High-Pressure Rotating Detonation Combustion in Rocket Environments (Ph.D. thesis), Purdue University; 2017.
[25] Burke R, Rezzag T, Dunn I, Flores W, Ahmed K. The effect of premixed stratification on the wave dynamics of a rotating detonation combustor. Int J Hydrog Energy 2021;46(54):27816–26.
[26] Xu S, Song F, Wu Y, Zhou J, Cheng P, Yang X, Chen X. Experimental investigation on combustion efficiency of a partially premixed kerosene-air rotating detonation combustor. Fuel 2022;329:125418.
[27] Zitoun R, Vidal P, Rodriguez V, Melguizo-Gavilanes J. A review of detonation studies applied to propulsion at Institute Pprime. In: Special international workshop on detonation for propulsion (IWDP). 2020.
[28] Goto K, Yokoo R, Kawasaki A, Matsuoka K, Kasahara J, Matsuo A, Funaki I, Kawashima H. Investigation into the effective injector area of a rotating detonation engine with impact of backflow. Shock Waves 2021;31(7):753–62.
[29] Nair AP, Lee DD, Pineda DI, Kriesel J, Hargus Jr. WA, Bennewitz JW, Bigler B, Danczyk SA, Spearrin RM. Methane-oxygen rotating detonation exhaust thermodynamics with variable mixing, equivalence ratio, and mass flux. Aerosp Sci Technol 2021;113:106683.
[30] Gao Y, Ng HD, Lee JH. Minimum tube diameters for steady propagation of gaseous detonations. Shock Waves 2014;24(4):447–54.
[31] Denisov YN, Troshin YK. Pulsating and spinning detonation of gaseous mixtures in tubes. Dokl Akad Nauk SSSR 1959;125:110–3.
[32] Voitsekhovskii B, Mitrofanov V, Topchian M. Trad: The structure of the detonation front in gases. SO AN SSSR 1963.
[33] Monnier V, Rodriguez V, Vidal P, Zitoun R. An analysis of three-dimensional patterns of experimental detonation cells. Combust Flame 2022;245:112310.
[34] Monnier V, Vidal P, Rodriguez V, Zitoun R. From graph theory and geometric probabilities to a representative width for three-dimensional detonation cells. Combust Flame 2023;256:112996.
[35] Aminallah M, Brossard J, Vasiliev A. Cylindrical detonations in methane-oxygen-nitrogen mixtures. Prog Astronaut Aeronaut 1993;153:203.
[36] Refloch A, Courbet B, Murrone A, Villedieu P, Laurent C, Gilbank P, Troyes J, Tessé L, Chaineray G, Dargaud J-B, Quémerais E, Vuillot F. CEDRE software. Aerosp Lab 2011;p. 1–10.
[37] Le Touze C, Murrone A, Guillard H. Multislope MUSCL method for general unstructured meshes. J Comput Phys 2015;284:389–418.
[38] Van Leer B. Towards the ultimate conservative difference scheme. II. Monotonicity and conservation combined in a second-order scheme. J Comput Phys 1974;14(4):361–70.
[39] Toro EF, Spruce M, Speares W. Restoration of the contact surface in the HLL-Riemann solver. Shock Waves 1994;4:25–34.
[40] Laurent C. low-order modeling and high-fidelity simulations for the prediction of combustion instabilities in liquid rocket engines and gas turbines (Ph.D. thesis), Toulouse, INPT; 2020.
[41] Sutherland W. LII. The viscosity of gases and molecular force. Lond Edinb Dublin Philos Mag J Sci 1893;36(223):507–31.
[42] Smagorinsky J. General circulation experiments with the primitive equations: I. The basic experiment. Mon Weather Rev 1963;91(3):99–164.
[43] Cocks PA, Holley AT, Greene CB, Haas M. Development of a high fidelity RDE simulation capability. In: 53rd AIAA aerospace sciences meeting. 2015, p. 1823.
[44] Hellard P, Gaillard T, Davidenko D, Zitoun R, Vidal P. Numerical investigation of the effects of friction and heat transfer on a non-premixed rotating detonation combustor operation. In: Proceeding of the European combustion meeting. 2023, p. 2112–7.
[45] Kessler DA, Gamezo VN, Oran ES. Gas-phase detonation propagation in mixture composition gradients. Philos Trans R Soc A 2012;370(1960):567–96.
[46] Boulal S, Vidal P, Zitoun R. Experimental investigation of detonation quenching in non-uniform compositions. Combust Flame 2016;172:222–33.
[47] Thomas G, Williams R. Detonation interaction with wedges and bends. Shock Waves 2002;11:481–92.
[48] Nakayama H, Moriya T, Kasahara J, Matsuo A, Sasamoto Y, Funaki I. Stable detonation wave propagation in rectangular-cross-section curved channels. Combust Flame 2012;159(2):859–69.
[49] Rodriguez V, Jourdain C, Vidal P, Zitoun R. An experimental evidence of steadily-rotating overdriven detonation. Combust Flame 2019;202:132–42.
[50] Lux J, Haidn O. Flame stabilization in high-pressure liquid oxygen/methane rocket engine combustion. J Propuls Power 2009;25(1):15–23.
[51] Fdida N, Vingert L, Mauriot Y, Dorey L-H, Théron M. Comparison of LOX/Methane and LOX/Hydrogen cryogenic spray combustion with simultaneous optical diagnostics. In: EUCASS 2019. 2019, p. 1–10.
[52] Kathrotia T. Reaction kinetics modeling of OH*, CH*, and C2* chemiluminescence (Ph.D. thesis), Ruprecht-Karls-Universität, Heidelberg; 2011.
[53] Paczko G, Lefdal PM, Peters N. Reduced reaction schemes for methane, methanol and propane flames. In: symposium (international) on combustion. Vol. 21, Elsevier; 1988, p. 739–48.
[54] Smith GP, Golden DM, Frenklach M, Moriarty NW, Eiteneer B, Goldenberg M, Bowman CT, Hanson RK, Song S, Gardiner Jr WC, Lissianski VV, Qin Z. http://www.me.berkeley.edu/gri_mech/.
[55] Nori VN, Seitzman JM. Ch* chemiluminescence modeling for combustion diagnostics. Proc Combust Inst 2009;32(1):895–903.
[56] Rankin BA, Richardson DR, Caswell AW, Naples AG, Hoke JL, Schauer FR. Chemiluminescence imaging of an optically accessible non-premixed rotating detonation engine. Combust Flame 2017;176:12–22.
[57] Nassini P. High-fidelity numerical investigations of a hydrogen rotating detonation combustor (Ph.D. thesis), University of Florence; 2022.
[58] Sutton GP, Biblarz O. Rocket propulsion elements. John Wiley & Sons; 2016.
[59] Goodwin DG, Moffat HK, Schoegl I, Speth RL, Weber BW. Cantera: An object-oriented software toolkit for chemical kinetics, thermodynamics, and transport processes. 2023, https://www.cantera.org, Version 3.0.0.
[60] Pal P, Kumar G, Drennan SA, Rankin BA, Som S. Multidimensional numerical modeling of combustion dynamics in a non-premixed rotating detonation engine with adaptive mesh refinement. J. Energy Resour Technol 2021;143(11):112308.
[61] Pal P, Demir S, Kundu P, Som S. Large-eddy simulations of methane-oxygen combustion in a rotating detonation rocket engine. In: AIAA propulsion and energy 2021 forum. 2021, p. 3642.
[62] Prakash S, Raman V, Lietz CF, Hargus Jr. WA, Schumaker SA. Numerical simulation of a methane-oxygen rotating detonation rocket engine. Proc Combust Inst 2021;38(3):3777–86.
[63] Strakey P, Ferguson DH. Validation of a computational fluid dynamics model of a methane-oxygen rotating detonation engine. In: AIAA scitech 2022 forum. 2022, p. 1113.
[64] Nassini PC, Andreini A, Bohon MD. Characterization of refill region and mixing state immediately ahead of a hydrogen-air rotating detonation using LES. Combust Flame 2023;258:113050.
[65] Cocks PA, Holley AT, Rankin BA. High fidelity simulations of a non-premixed rotating detonation engine. In: 54th AIAA aerospace sciences meeting. 2016, p. 0125.
[66] Petersen EL, Davidson DF, Hanson RK. Kinetics modeling of shock-induced ignition in low-dilution CH4/O2 mixtures at high pressures and intermediate temperatures. Combust Flame 1999;117(1-2):272–90.
[67] Zhukov VP, Kong AF. A compact reaction mechanism of methane oxidation at high pressures. Prog React Kinet Mech 2018;43(1):62–78.
[68] Chemical-kinetic mechanisms for combustion applications, Mechanical and Aerospace Engineering (Combustion Research), University of California at San Diego, http://web.eng.ucsd.edu/mae/groups/combustion/mechanism.html, 2016.